Available online at www.sciencedirect.com
SCIENCE DIRECT®
International Journal of Heat and Mass Transfer 47 (2004) 4153–4164
International Journal of HEAT and MASS TRANSFER
www.elsevier.com/locate/ijhmt

Numerical modeling of scanning laser-induced melting, vaporization and resolidification in metals subjected to step heat flux input

Haseung Chung, Suman Das *

Department of Mechanical Engineering, University of Michigan, 2250 GG Brown, 2350 Hayward Street, Ann Arbor, MI 48109-2125, USA

Received 20 March 2004; received in revised form 6 May 2004
Available online 2 July 2004

Abstract

We present a 1-D heat transfer, melting, vaporization and resolidification model describing the interaction of a scanning continuous-wave laser with a metal surface wherein the beam power is constant. A physical model based on the Stefan problem is developed with appropriate boundary conditions. The effects of processing parameters on process variables are investigated numerically by varying beam diameters, scan speeds and substrate temperatures for Nickel. Relations are derived for the times to initiate melting, to initiate vaporization, to reach maximum melting depth, for melting-resolidification, and for maximum melting and vaporization depths. Surface temperatures are compared with approximate closed form solutions.

Keywords: Laser processing; Melting; Vaporization; Resolidification; Stefan problem

1. Introduction

Selective laser sintering (SLS) [13] is a solid freeform fabrication technique that creates three dimensional freeform objects directly from their CAD models. An object is created by selectively fusing thin layers of a powder using a computer-controlled scanning laser beam that scans patterns corresponding to slices of the CAD model. In contrast with SLS of amorphous polymeric materials where the powder undergoes sintering and partial densification, direct SLS of metals is a process in which a high-energy laser beam scans, melts and consolidates a metal powder or powder mixture to full or near-full density. This is a complex process exhibiting multiple modes of heat and mass transfer. The inherent complexity of this process requires the construction of increasingly sophisticated models to enable a fundamental understanding of the important underlying physical mechanisms. This understanding is essential to implement effective process control schemes [12]. In order to understand and control this process, detailed knowledge of the spatial and temporal characteristics of temperature and melt interface is required as a function of controllable processing parameters. These parameters include input laser power (typically 0.1–1 kW), focused beam diameter (typically 100–500 μm) and beam scan speed (typically 0.1–10 m/s). In direct SLS, metal powders melt after absorbing a large amount of heat from the laser beam and then release the heat during resolidification to form fully dense shapes. Melting and resolidification processes have a significant influence on the temperature distribution, residual stress, and the final microstructure quality of the parts. Neglecting such important effects could result in significant errors in thermal modeling [37]. In other words, understanding dynamics of phase change processes during laser melting is essential to obtaining high quality parts especially

* Corresponding author. Tel.: +1-734-615-6646; fax: +1-734-647-3170.
E-mail address: sumandas@umich.edu (S. Das).

0017-9310/$ - see front matter © 2004 Elsevier Ltd. All rights reserved.
doi:10.1016/j.ijheatmasstransfer.2004.05.003

Nomenclature

B_f	boundary heat flux factor
c_p	specific heat
D	solid–liquid thermal diffusivity ratio
d	beam diameter
Fo	Fourier number ($=\frac{\alpha_s t}{r^2}$)
k	thermal conductivity
L	domain length
P	laser power
Q_s	supplied total energy density ($=\frac{4P}{\pi dv}$, step heat flux input)
q''	laser heat flux
R_f	boundary radiation heat flux factor
r	beam radius
St	Stefan number
T_i	initial temperature
T_m	melting temperature
T_∞	ambient temperature
T_v	vaporization temperature
T_s	surface temperature
t_i	time to initiate melting
t_{vi}	time to initiate vaporization
t_{max}	time to reach maximum melt depth
t_{tot}	total melting-resolidification time
V	velocity of solid–liquid interface
V_v	velocity of liquid–vapor interface
v	beam scan speed
x	dimensional coordinate
$x_{f,max}$	maximum melt depth
$x_{vf,max}$	maximum vaporization depth

Greek symbols

α_a	optical absorptivity
α	thermal diffusivity
γ	ratio of latent heat of fusion to latent heat of evaporation
Δ	dimensionless beam diameter
ϵ	optical emissivity
ζ_{max}	dimensionless maximum melting depth
$\zeta_{v,max}$	dimensionless maximum vaporization depth
η	dimensionless beam speed
θ	dimensionless temperature
θ_v	dimensionless vaporization temperature
θ_i	dimensionless initial temperature
θ_s	dimensionless surface temperature
κ	solid to liquid thermal conductivity ratio
λ	latent heat of fusion
λ_v	latent heat of evaporation
ξ	dimensionless time ($=\frac{t}{\tau}$)
ρ	material density
σ	Stefan–Boltzmann constant
τ	beam–material interaction time
τ_i	dimensionless time to initiate melting
τ_{vi}	dimensionless time to initiate vaporization
τ_{int}	dimensionless beam–material interaction time
τ_{max}	dimensionless time to reach maximum melting depth
τ_{tot}	dimensionless time for melting and resolidification
ϕ	dimensionless absorbed laser energy density
χ	dimensionless coordinate

Subscripts

s	solid
l	liquid
f	solid–liquid interface
vf	liquid–vapor interface

when higher-order laser scanning paths beyond conventional straight line raster scanning are utilized. Processes involving laser based fusion need real-time control strategies that incorporate melt dynamics. However, current direct SLS processing lacks melt-depth dynamic control capability. Therefore, when higher-order scanning paths are used, the power or speed of the laser beam must be manually adjusted along the path to provide sufficient depth of melt [1]. In order to implement real-time laser power, beam diameter, and scan speed control, there exists a need to understand the response of melting, vaporization and resolidification processes to time-dependent changes in laser power input. This is especially necessary to account for process perturbations that occur due to deliberate or random fluctuations in laser power, due to different boundary conditions that occur during the layer-by-layer fabrication process where a layer of powder could have a previously solidified layer surface underneath (conducting) versus just powder underneath (relatively insulating), as well as to account for variations in thermophysical, optical and material properties when multiple materials are used to make heterogeneous parts. In our first attempt to address the above needs, in this paper, we present a one-dimensional model that describes the physical mechanisms of heat transfer, melting, vaporization and resolidification taking place during and after the interaction of a quasi-stationary laser beam with a metal substrate. The substrate interacting with the laser is treated as a crystalline surface with a sharp melting and vaporization temperature. Although our intent is to understand such phenomena occurring in direct SLS

where a laser beam interacts with a metal powder bed, the model developed here is applicable in general to laser melting of metals, provided the 1-D assumption is met and boundary conditions are satisfied. The problem is treated in dimensionless form enabling a parametric analysis under various processing conditions.

2. Background

A review of the literature shows several works investigating the one-dimensional melting of metals. A study by Cohen [10] was motivated by a need for understanding the mechanisms of melting and vaporization of materials subjected to heat fluxes produced by various sources. Towards this end, a solution technique capable of treating time-varying heat inputs as well as the step-function heat input was developed. Zien [40] presented approximate solutions for the one-dimensional transient ablation problem with two specific forms of time-dependent boundary heat flux based on Landau's [19] idealized ablation model including power-law boundary heat flux and exponential boundary heat flux. Sharma et al. [26] described simplified procedures for the approximate solution of heat-transfer problems with phase change for time-dependent surface temperatures, showing comparisons between approximate solutions and numerical solutions. Cline and Anthony [9] derived a thermal analysis for laser heating and melting materials for a Gaussian heat source moving at a constant velocity. They concluded that the resulting temperature distribution, cooling rate distribution, and depth of melting was related to the laser spot size, velocity, and power level. Bertolotti and Sibilia [3] suggested analytical solutions for the penetration of a laser heat flux-induced melting front by solving the motion equation of the fusion interface, obtained by the conduction heat equation for the liquid region, and by the energy conservation at the fusion front. Solutions were obtained both for uniform and Gaussian intensity distribution laser beams and also for the case of constant thermal properties, while introducing the thermal conductivity discontinuity at the fusion interface. In the paper by El-Adawi and Elshehawey [14], the problem of heating a homogeneous slab of material by time-dependent laser irradiance was studied. They also obtained an exact solution for the temperature distribution of the slab by the Fourier series expansion technique. Pak and Plumb [20] examined a one-dimensional, phase-change process in a two-component packed bed. The macroscopic energy equation and continuity equations for both the liquid and solid phases were solved numerically, and experiments were conducted to confirm the numerical results. Ho and Grigoropoulos [15] solved the heat conduction in the solid substrate and in the liquid melt by a one-dimensional transient heat transfer model. Xu et al. [34] developed a conductive heat transfer model including the analysis of melting and resolidification by applying an interface tracking finite difference algorithm to calculate the melt front propagation and the transient temperature field in Silicon. Zhang and Faghri [36] investigated the effects of moving heat source intensity and the scanning velocity on the sintering depth, the location and shape of the liquid pool in a two component metal powder bed comprising two metals of vastly differing melting temperatures. Zhang and Faghri [38] also studied melting and vaporization phenomena during the laser drilling process. Xie and Kar [33] examined the melting rate during laser materials processing with a one-dimensional heat conduction model, yielding approximate correlations for time dependence of melt depth as well as average melting velocity as functions of linear power density, thermophysical properties and melt temperature. Ahn et al. [1] suggested approximate solutions for a transient one-dimensional heat conduction problem with a moving heat source and moving phase boundary by three different methods. Shiomi et al. [27] simulated the melting and solidifying processes of metallic powders by the finite element method. Wood and Geist [32] developed a computational model for treating various aspects of the complex melting and solidification phenomena in pulsed-laser irradiated materials. Wang et al. [29,30] suggested an effective interface-tracking scheme for the numerical modelling of heat transfer and phase change during rapid solidification. Wang et al. [31] also conducted a dimensionless analysis of controlling parameters under various conditions. Huang et al. [16] described a model for melting and solidification of thin wires and Chung and Das [8] presented a one-dimensional model describing melting and resolidification during and after the interaction of a laser beam with semi-infinite metal surface. Besides these, numerous studies on heat conduction involving phase change and moving heat sources were done [18,22,24,28,35,39]. The aforementioned studies modeled either melting only, melting with vaporization, or melting with subsequent resolidification but without vaporization. However, understanding and predicting melting, vaporization and resolidification processes as a function of time-varying laser power input are important for real-time control of laser fusion based material processing. Furthermore, dimensionless analyses of scaling laws relating process variables to controllable process parameters in such processes are especially useful in understanding process dynamics. To our knowledge, the work presented in this article is the first attempt at 1-D modeling of combined melting, vaporization and resolidification and also the first to derive such scaling laws. In the future these laws could be incorporated into solidification models that can predict microstructure formation as a function of processing parameters.

3. Physical model

In this paper, we consider one-dimensional heat conduction with phase change in a solid of length L, $L \gg d$ where d is the laser beam diameter. Heat flux from a continuous wave laser flows in through the top surface during heat up while the bottom surface is assumed insulated. If heating continues long enough, melting commences at temperature T_m and the melt interface moves inward. Furthermore, if surface temperature reaches vaporization temperature T_v, vaporization is initiated and liquid–vapor interface also moves inward. After heat flux q'' is turned off at time τ, heat is lost during cool down from the top surface only by radiation to the ambient at temperature T_∞. We aim to determine the time to initiate melting, time to initiate vaporization, time to reach the maximum melting depth, total time for melting and resolidification, as well as the temperature distribution, the velocity and the location of the melt interface within the domain of interest. The governing equations were non-dimensionalized with the following simplifying assumptions. Powder is treated as a solid substrate at uniform initial temperature with no volumetric sintering densification during the process. Laser beam intensity distribution is assumed uniform across the beam diameter d and incident laser heat flux q'' is absorbed at the surface with optical absorptivity α_a. Material properties for each phase are assumed independent of temperature. Density is assumed constant and same for both solid and liquid phases. Convective heat transfer at the top surface is neglected. The process is assumed to occur in an inert atmosphere at 1 atm ambient pressure [11]. Further, the vaporization temperature is assumed to be equal to the saturation temperature at ambient pressure. Melt pool convection and convective heat transfer at the melt interface are also neglected. The melt interface and liquid–vapor interface are assumed to propagate in a planar fashion and the top surface is assumed to be diffuse and gray. In order to satisfy the one-dimensional approximation, the beam–material interaction time ($\tau = \frac{d}{v}$), defined as the time taken by the scanning beam with velocity v to traverse one beam diameter, should be small compared to the radial thermal diffusion time in the solid of thermal diffusivity α_s. In dimensionless form,

$$\tau_{\text{int}} = \frac{d}{v} \Big/ \frac{(d/2)^2}{\alpha_s} \ll 1 \tag{1}$$

$$\therefore v \gg \frac{4\alpha_s}{d} \tag{2}$$

The 1-D heat equation with constant properties describing the process is:

$$\frac{\partial^2 T}{\partial x^2} = \frac{1}{\alpha}\frac{\partial T}{\partial t} \tag{3}$$

The boundary condition at the top surface is

$$-k\frac{\partial T}{\partial x} = \alpha_a q'' + \varepsilon\sigma\left(T_\infty^4 - T^4\right), \quad x = x_{vf}, \quad T_s < T_v \tag{4}$$

while the boundary condition at the bottom surface assumed insulated is

$$-k\frac{\partial T}{\partial x} = 0, \quad x = L \tag{5}$$

and the initial condition is

$$T = T_i, \quad 0 \leqslant x \leqslant L \tag{6}$$

The Stefan condition describing the heat flux balance at the planar melt interface is

$$k_s\frac{\partial T}{\partial x}\bigg|_s - k_l\frac{\partial T}{\partial x}\bigg|_l = \rho V\lambda, \quad x = x_f \tag{7}$$

and energy conservation equation at the planar liquid–vapor interface is

$$\alpha_a q'' + \varepsilon\sigma\left(T_\infty^4 - T^4\right) + k_l\frac{\partial T}{\partial x}\bigg|_l = \rho V_v\lambda_v, \quad x = x_{vf}, \quad T_s \geqslant T_v \tag{8}$$

where P is the laser power, $q''(t) = \frac{4P}{\pi d^2}$ is the step heat flux ($0 \leqslant t \leqslant \tau$), ρ is the material density, V is the velocity of the solid–liquid interface, V_v is the velocity of the liquid–vapor interface, λ is the latent heat of fusion, λ_v is the latent heat of evaporation, x_f is the location of the melt interface, x_{vf} is the location of the liquid–vapor interface, $c_{pi}, i = s, l$ are the specific heat capacities of the solid and liquid respectively.

These equations are non-dimensionalized using the following normalized variables: temperature $\theta = \frac{T-T_\infty}{T_m-T_\infty}$, surface temperature $\theta_s = \frac{T_s-T_\infty}{T_m-T_\infty}$, vaporization temperature $\theta_v = \frac{T_v-T_\infty}{T_m-T_\infty}$, coordinate $\chi = \frac{x}{r} = \frac{2x}{d}$, melt interface location $\chi_f = \frac{x_f}{r} = \frac{2x_f}{d}$, liquid–vapor interface location $\chi_{vf} = \frac{2x_{vf}}{d}$, time $\xi = \frac{t}{\tau}$, beam speed $\eta = \frac{v\tau}{\alpha_s} = \frac{vd}{2\alpha_s}$, Stefan number $St = \frac{c_{ps}(T_m-T_\infty)}{\lambda}$, solid–liquid thermal diffusivity ratio $D = \frac{\alpha_s}{\alpha_l}$, solid–liquid thermal conductivity ratio $\kappa = \frac{k_s}{k_l}$, latent heat of fusion to latent heat of evaporation ratio $\gamma = \frac{\lambda}{\lambda_v}$. We also define a boundary heat flux factor $B_f = \frac{\alpha_a d c_{ps} q''}{2k_s\lambda}$ and a boundary radiation heat flux factor $R_f = \frac{\varepsilon d c_{ps}\sigma(T^2+T_\infty^2)(T+T_\infty)(T_m-T_\infty)}{2k_s\lambda}$. Using these variables, the non-dimensionalized governing equations are stated as follows:

The heat equation,

$$\frac{\partial^2\theta}{\partial\chi^2} = \frac{\eta}{2}\frac{\partial\theta}{\partial\xi}, \chi < \chi_f \tag{9}$$

$$= \frac{\eta}{2}D\frac{\partial\theta}{\partial\xi}, \chi \geqslant \chi_f \tag{10}$$

with the boundary conditions:

At $\chi = \chi_{vf}$,

$$\frac{\partial\theta}{\partial\chi} = -\frac{B_f}{St} + \frac{R_f}{St}\theta, \quad \theta < 1, \theta_s < \theta_v \tag{11}$$

$$= -\frac{B_f}{St}\kappa + \frac{R_f}{St}\kappa\theta, \quad \theta \geqslant 1, \theta_s < \theta_v \tag{12}$$

while at $\chi = \frac{2L}{d}$

$$\frac{\partial\theta}{\partial\chi} = 0 \tag{13}$$

The initial condition is

$$\theta = \theta_i, \quad 0 \leqslant \chi \leqslant \frac{2L}{d} \tag{14}$$

and the Stefan condition at the solid–liquid interface,

$$\left.\frac{\partial\theta}{\partial\chi}\right|_s - \frac{1}{\kappa}\left.\frac{\partial\theta}{\partial\chi}\right|_l = \frac{\eta}{2St}\frac{\partial\chi}{\partial\xi} \tag{15}$$

Also, energy conservation equation at the liquid–vapor interface is

$$\frac{\kappa B_f}{St} - \frac{\kappa R_f}{St}\theta + \left.\frac{\partial\theta}{\partial\chi}\right|_l = \frac{\kappa\eta}{2\gamma St}\frac{\partial\chi}{\partial\xi}, \quad \theta_s \geqslant \theta_v \tag{16}$$

We define t_i as the time to initiate melting, t_{vi} the time to initiate vaporization, t_{max} the time to reach maximum melt depth, t_{tot} the total melting-resolidification time, $x_{f,max}$ the maximum melt depth, $x_{vf,max}$ the maximum vaporization depth, $\alpha_a q''\tau$ the absorbed laser energy density, and their dimensionless counterparts $\tau_i = \frac{\alpha_s t_i}{L^2}$, $\tau_{vi} = \frac{\alpha_s t_{vi}}{L^2}$, $\tau_{max} = \frac{\alpha_s t_{max}}{L^2}$, $\tau_{tot} = \frac{\alpha_s t_{tot}}{L^2}$, $\zeta_{max} = \frac{x_{f,max}}{L}$, $\zeta_{v,max} = \frac{x_{vf,max}}{L}$, $\phi = B_f \cdot \tau_{int} = \frac{2\alpha_a q''}{\rho v \lambda}$ respectively.

4. Numerical scheme

There are two widely used methods in the fixed grid solution for phase change problems, namely enthalpy methods and temperature-based equivalent heat capacity methods. Enthalpy methods are flexible and can deal with phase change problems occurring both at a single temperature and over a temperature range [25,4]. However, these methods have the shortcoming that although the predicted temperature distributions and melting fronts are reasonable, the predicted time history of the temperature at a typical grid point may have some oscillations. The temperature-based fixed grid methods have no such time history problems and are more convenient with conjugate problems involving an adjacent wall, but have to handle the severe nonlinearity of the governing equations when phase change temperature range is small [6]. On the other hand, front tracking schemes attempt to explicitly track the interface using the Stefan condition [17]. While one approach is to fix the spatial step but allow the time step to float in such a way that the front always passes through a node, another approach is to fix the time step and allow the spatial step to float, using two distinct, time-varying spatial steps for the two phases. Although such approaches work fairly well for a simple Stefan problem, difficulties arise when the entire domain is at the same initial temperature, far below melting temperature because a priori knowledge of initial melt interface location is required [2]. In this work, we developed a front tracking scheme with fixed grid and fixed time step based on a finite volume method [21,7]. An explicit discretization scheme (first order in time domain, second order in space domain) satisfying stability criteria was employed. The accuracy of this method is verified via comparison with closed form solutions for surface temperature as a function of time [23].

5. Simulation parameters

Numerical computations were conducted for step heat flux input (constant laser power P during $0 \leqslant t \leqslant \tau$ followed by a drop to zero power). The concept of beam–material interaction time τ is used to simulate the temporal action of a moving laser beam over a surface area corresponding to one beam diameter, and can be used to set the duration for heat flux input experienced by an area of the surface corresponding to one beam diameter. Computations were carried out for 10 different beam diameters with 4 different scan speeds. Therefore, step power input was tested for 40 different beam–material interaction times. In order to investigate the effect of substrate initial temperature, five initial substrate temperatures at a fixed beam diameter ($d =$ 200 μm) and scan speed ($v = 1.0$ m/s) were also tested. The material properties of Nickel [31] were used for computations. Table 1 shows beam diameters and scan speeds selected for the computations, satisfying the 1-D approximation. Other parameter values used for the computations are shown in Table 2.

The computations yielded temperature histories, interface locations, and interface velocities as functions of time and processing parameters. Further, relations between dimensionless process variables τ_i, τ_{max}, τ_{tot} and

Table 1
Parameters used for numerical computations I

Diameter (μm)	80	100	150	200	250	300	350	400	450	500
Scan speed (m/s)	1.0	1.0	0.5	0.5	0.5	0.5	0.5	0.5	0.5	0.5
	2.5	2.5	0.75	0.75	0.75	0.75	0.75	0.75	0.75	0.75
	5.0	5.0	1.0	1.0	1.0	1.0	1.0	1.0	1.0	1.0
	7.5	7.5	1.25	1.25	1.25	1.25	1.25	1.25	1.25	1.25

Table 2
Parameters used for numerical computations II

Domain size	Number of nodes	Time step	Laser beam power
5 mm	500	1×10^{-8} s	1000 W

ζ_{max}, and controllable process parameters τ_{int} and input laser heat flux q'' were developed. These relations are discussed in the following sections.

6. Results and discussion

6.1. Time to initiate melting

Fig. 1(a) and (b) are a set of plots showing τ_i, the dimensionless time to initiate melting versus τ_{int}, the dimensionless beam–material interaction time and τ_i versus ϕ, the dimensionless energy density respectively, for fixed beam diameters ranging from 80 to 500 μm. Both figures show that for fixed beam diameter, τ_i is constant and independent of τ_{int} and ϕ. At each fixed beam diameter, although τ_{int} and ϕ can vary, the input heat flux q'' remains constant and primarily determines τ_i.

Fig. 1(c) is a plot of τ_i versus τ_{int} for fixed scan speeds ranging from 0.5 to 1.25 m/s. This plot shows that for each fixed scan speed, τ_i increases as τ_{int} decreases (beam diameter increases), and as the input heat flux q'' decreases. We also note that as the beam diameter increases, τ_i increases nonlinearly due to the inverse square dependence of heat flux on diameter. From these observations, a scaling law relating τ_i and normalized beam diameter $(\Delta = d/L)$ can be obtained with an

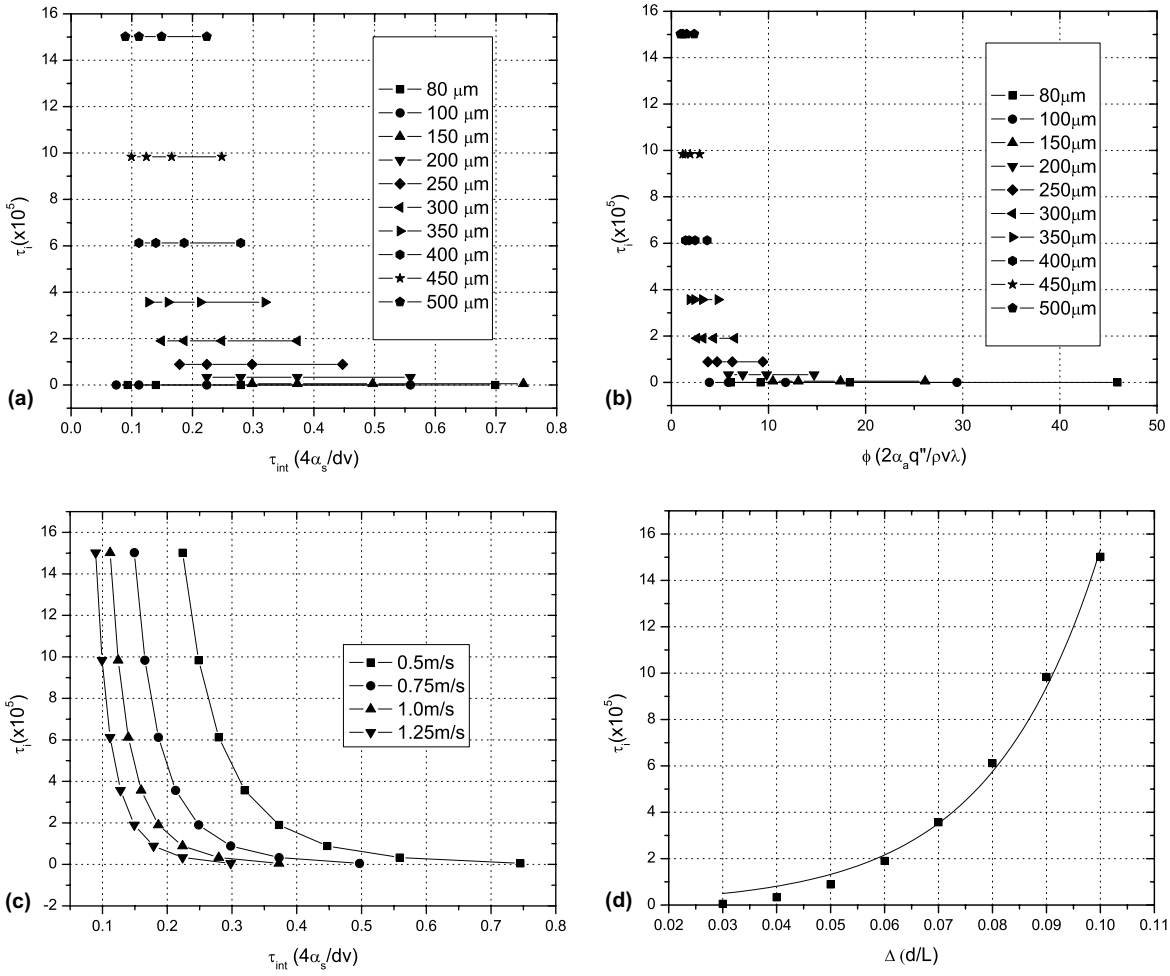

Fig. 1. (a) Dimensionless time to initiate melting vs. dimensionless beam–material interaction time at fixed beam diameters, (b) dimensionless time to initiate melting vs. dimensionless energy density at fixed beam diameters, (c) dimensionless time to initiate melting vs. dimensionless beam–material interaction time at fixed scan speeds, and (d) dimensionless time to initiate melting vs. normalized beam diameter.

exponential fit yielding $\tau_i = 1.14 \times 10^{-6} e^{49.012\Delta}$ with $R^2 = 0.99$ (150 μm $< d <$ 500 μm) as shown in Fig. 1(d). This law predicts that doubling the beam diameter, for example from 200 to 400 μm increases the time to initiate melting by nearly three orders of magnitude from 5.9 μs to 0.11 ms.

6.2. Time to initiate vaporization

Fig. 2(a) is a plot of τ_{vi}, the dimensionless time to initiate vaporization versus τ_{int} for fixed beam diameters ranging from 80 to 500 μm. This plot shows that for fixed beam diameter, τ_{vi} is constant and independent of τ_{int}. However, for beam diameters larger than 400 μm some cases do not exhibit vaporization. As τ_{int} decreases (scan speed increases) for fixed beam diameter, supplied total energy density Q_s $(= \frac{4P}{\pi dv})$ decreases. This result indicates that a minimum supplied total energy density is needed for vaporization to occur.

Fig. 2(b) shows τ_{vi} as a decreasing function of ϕ for fixed scan speeds. For fixed scan speed, beam–material interaction time is linearly proportional to diameter, while heat flux input is inversely proportional to the diameter squared. Thus, the variation of τ_{vi} is dominated by supplied total energy density.

6.3. Time to reach maximum melting depth

Fig. 2(c) shows τ_{max}, the dimensionless time to reach maximum melting depth as a function of τ_{int} for fixed beam diameters. For each fixed beam diameter, τ_{max} is nearly a linearly increasing function of τ_{int} (inversely proportion to scan speed) while the slope of τ_{max} vs. τ_{int} is a increasing function of beam diameter. For fixed τ_{int},

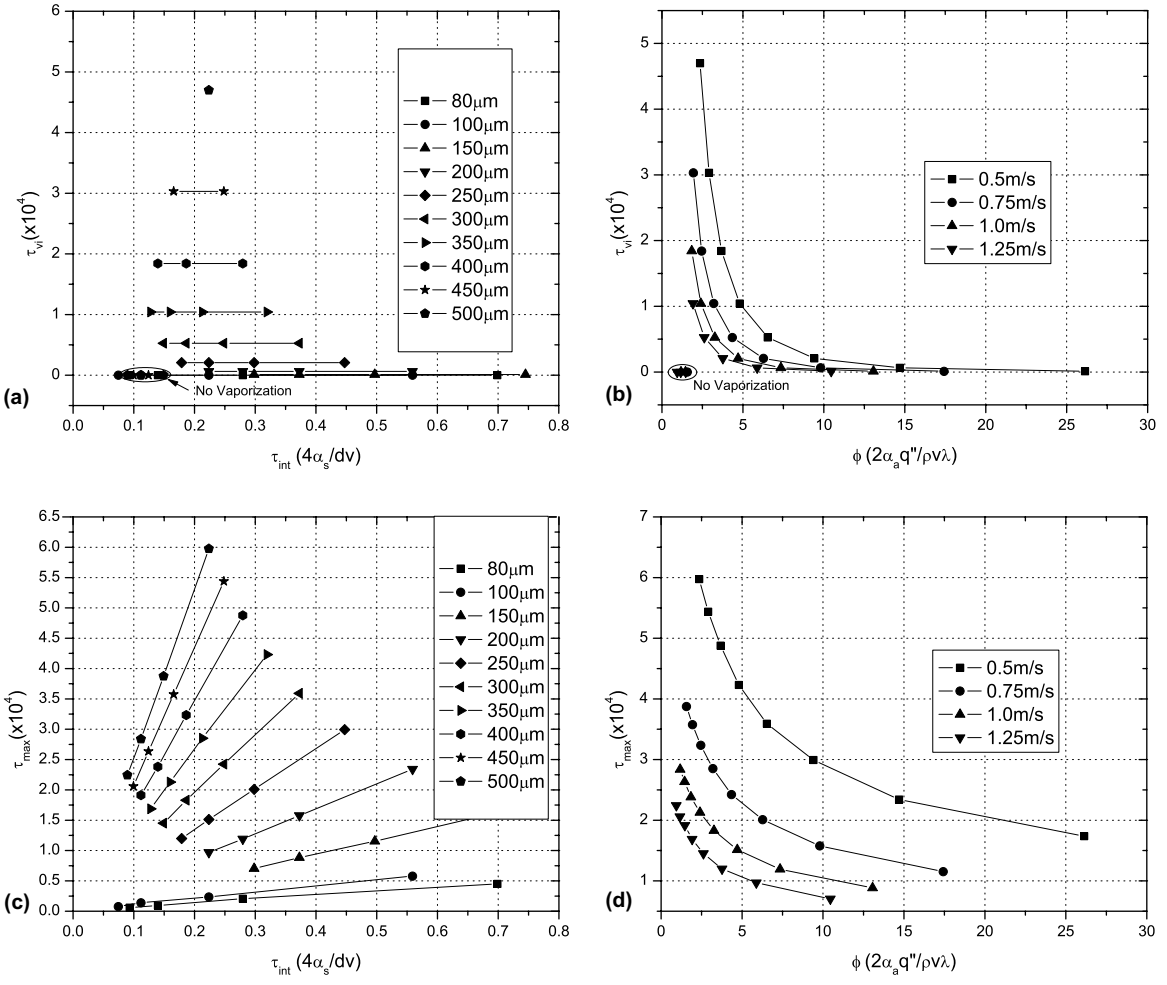

Fig. 2. (a) Dimensionless time to initiate vaporization vs. dimensionless beam–material interaction time at fixed beam diameters, (b) dimensionless time to initiate vaporization vs. dimensionless energy density at fixed scan speeds, (c) dimensionless time to reach maximum melting depth vs. dimensionless beam–material interaction time at fixed beam diameters, and (d) dimensionless time to reach maximum melting depth vs. dimensionless energy density at fixed scan speeds.

τ_{max} increases with increasing beam diameter. This results from the fact that although the supplied total energy density remains constant, beam–material interaction time τ increases as beam diameter increases for fixed τ_{int}.

Fig. 2(d) shows τ_{max} as a function of ϕ for a range of fixed scan speeds. For each fixed scan speed, as ϕ increases, τ_{max} decreases. While heat flux input is inversely proportional to beam diameter squared, beam–material interaction time is linearly proportional to beam diameter for fixed scan speeds. As beam diameter increases for fixed scan speeds, τ_{max} decreases due to decreasing heat flux input and increasing beam–material interaction time.

6.4. Time for melting and resolidification

Fig. 3(a) is a plot of τ_{tot}, the dimensionless time for melting and resolidification versus τ_{int} for fixed beam diameters. This plot shows that for a fixed diameter, τ_{tot} decreases with decreasing τ_{int} (increasing scan speed). This results from the decrease in beam–material interaction time and the consequent decrease in the supplied total energy density as scan speed increases. The slope of τ_{tot} vs. τ_{int} is a increasing function of beam diameter just as it is in the case of time to reach maximum melting depth.

Fig. 3(b) shows τ_{tot} as a function of ϕ for fixed scan speeds. The dotted line separates those cases where no vaporization occurs from those in which there is some vaporization. If there is no vaporization, τ_{tot} increases with increasing ϕ. As ϕ increases (beam diameter decreases), the beam–material interaction time τ decreases but supplied total energy density increases (owing to the inverse square dependence of q'' on diameter). This implies that dominant factor influencing τ_{tot} in the absence of vaporization is the supplied total energy density.

However, when vaporization occurs, some material is ablated and this affects τ_{tot}. In such cases, the influence of ϕ is reversed. In other words, for cases with vaporization, at fixed scan speed, τ_{tot} decreases with increasing ϕ. Therefore, the onset of vaporization reverses τ_{tot} from an increasing function of ϕ to a decreasing one.

6.5. Maximum melting depth

Fig. 3(c) shows ζ_{max}, the dimensionless maximum melting depth as a function of τ_{int} for fixed beam diameters. For each fixed diameter, ζ_{max} decreases as scan speed increases, resulting in the decrease of both beam–material interaction time and supplied total energy density.

Fig. 3(d) shows ζ_{max} as a function of ϕ for fixed scan speeds. For each fixed scan speed, ζ_{max} increases with ϕ (decreasing beam diameter). As beam diameter decreases, beam–material interaction time τ decreases but supplied total energy density ($= \frac{4P}{\pi d v}$) increases. The dotted line separates those cases where no vaporization occurs from those in which some vaporization is present. For each fixed scan speed, a steep gradient for ζ_{max} versus ϕ in the absence of vaporization is smoothened with the onset of vaporization. Therefore, the supplied total energy density is the dominant factor controlling ζ_{max}.

6.6. Maximum vaporization depth

Fig. 4(a) shows $\zeta_{v,max}$, the dimensionless maximum vaporization depth as a function of τ_{int} for fixed beam diameters. For each fixed diameter, $\zeta_{v,max}$ decreases as scan speed increases, resulting in the decrease of both beam–material interaction time and supplied total energy density. However some cases do not experience vaporization. This result indicates that a minimum supplied total energy density is needed for vaporization.

Fig. 4(b) shows $\zeta_{v,max}$ as a function of ϕ for fixed scan speeds. When vaporization occurs, $\zeta_{v,max}$ increases with ϕ (decreasing beam diameter) for each fixed scan speed. While beam–material interaction time τ is linearly proportional to beam diameter, heat flux input is inversely proportional to the diameter squared for fixed scan speed. The slope of $\zeta_{v,max}$ vs. ϕ is a weakly decreasing function of scan speed. Therefore, the supplied total energy density is also dominant factor controlling $\zeta_{v,max}$.

6.7. Initial substrate temperature and surface temperature

Fig. 4(c) shows ζ_{max} as a function of dimensionless initial substrate temperature θ_i for $d = 200$ μm, $v = 1.0$ m/s. As substrate temperature increases, ζ_{max} increases as expected since lesser laser energy needs to be supplied to raise the temperature to the melting point and consequently the melt interface penetrates deeper. Scaling laws for τ_i, τ_{vi}, τ_{max}, τ_{tot}, ζ_{max} and $\zeta_{v,max}$ in terms of θ_i were also derived and are shown in Table 3. τ_i and τ_{vi} are decreasing functions of θ_i, while τ_{max}, τ_{tot}, ζ_{max} and $\zeta_{v,max}$ are increasing ones as expected.

A comparison of our numerical solution for surface temperature as a function of time against Prokhorov's [23] approximate closed form solution was investigated. Fig. 4(d) compares the numerical solution and approximate closed form solution of dimensionless surface temperature $\theta_s = \frac{T_s - T_\infty}{T_m - T_\infty}$ versus dimensionless time (Fourier number, Fo) for the case of $d = 200$ μm beam diameter and $v = 1.0$ m/s scan speed. Prokhorov's closed form solution estimates a higher peak surface temperature compared with our numerical solution. This result can be attributed to two probable causes. First, our model includes vaporization while Prokhorov's does not. Second, our model incorporates the appropriate thermal diffusivities for Nickel in the solid and liquid states while Prokhorov assumes a constant diffusivity

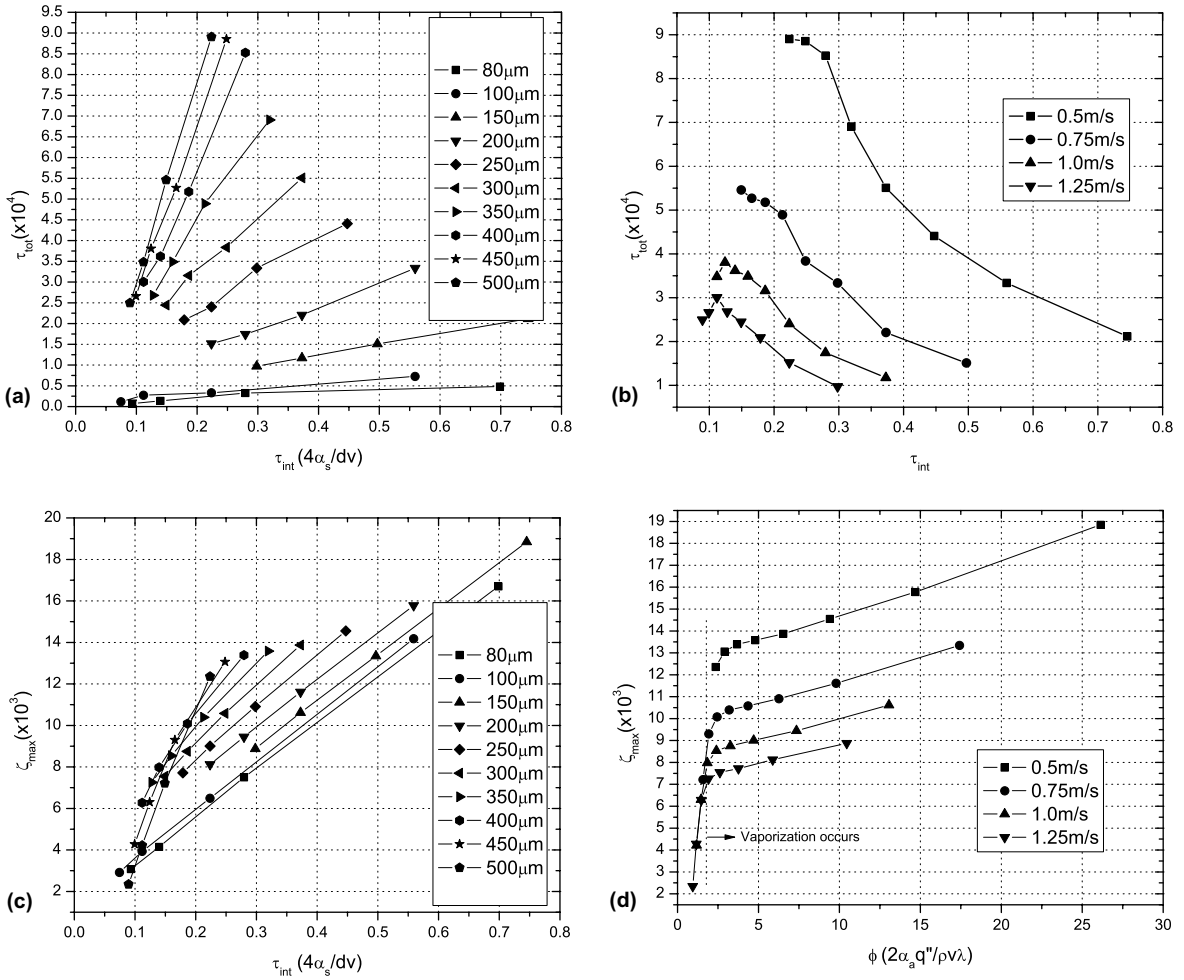

Fig. 3. (a) Dimensionless time for melting and resolidification vs. dimensionless beam–material interaction time at fixed beam diameters, (b) dimensionless time for melting and resolidification vs. dimensionless energy density at fixed scan speeds, (c) dimensionless maximum melting depth vs. dimensionless beam–material interaction time at fixed beam diameters, and (d) dimensionless maximum melting depth vs. dimensionless energy density at fixed scan speeds.

corresponding to the solid state. Note that the thermal diffusivity of liquid Nickel is lower than that of solid Nickel. These differences reflect the effects of the latent heat of vaporization and material properties for liquid and solid states included in our numerical solution but neglected in Prokhorov's closed form solution. This was also investigated elsewhere [5].

7. Summary and conclusions

A dimensionless analysis of the controlling parameters under various conditions including different beam diameters, scan speeds, and substrate temperatures was conducted. Using a one-dimensional approximation, this model provides insights into the characteristics of time to initiate melting, time to initiate vaporization, time to reach the maximum melting depth, total time for melting and resolidification, maximum melting depth and maximum vaporization depth for a step heat flux input. A summary of our findings is presented in Table 4. We observed that τ_i and τ_{vi} are inversely proportional to heat flux input and supplied total energy density respectively, in the presence of vaporization. We find that τ_{max} is proportional to beam–material interaction time. τ_{tot} is a increasing function of supplied total energy density for fixed beam diameter and for fixed scan speed in the absence of vaporization. However, τ_{tot} decreases as ϕ increases for fixed scan speed in the presence of vaporization. Both ζ_{max} and $\zeta_{v,max}$ are proportional to the supplied total energy density. Scaling laws were derived for τ_i, τ_{vi}, τ_{max}, τ_{tot}, ζ_{max} and $\zeta_{v,max}$ as functions of

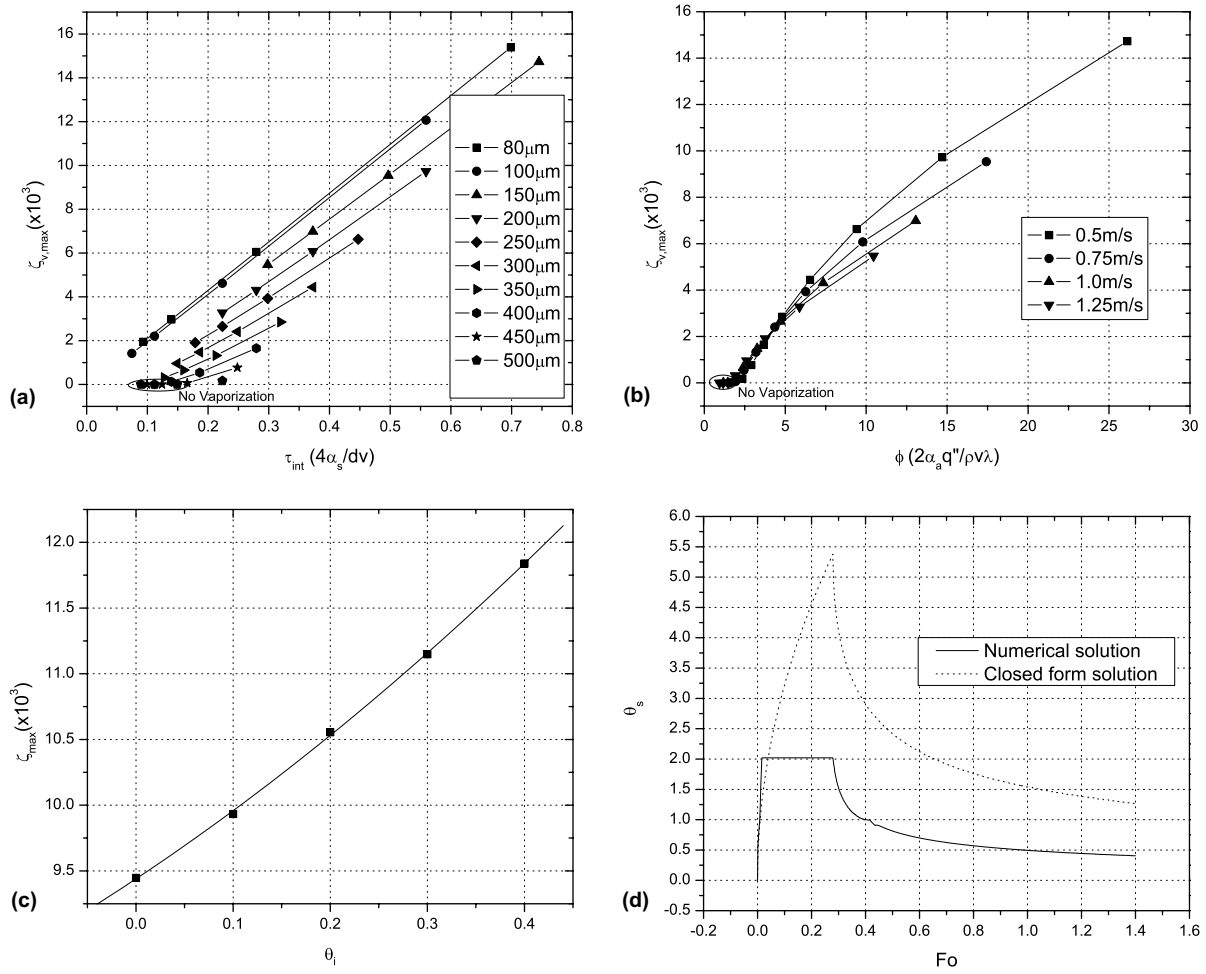

Fig. 4. (a) Dimensionless maximum vaporization depth vs. dimensionless beam–material interaction time at fixed beam diameters, (b) dimensionless maximum vaporization depth vs. dimensionless energy density at fixed scan speeds, (c) dimensionless maximum melting depth vs. dimensionless initial substrate temperature ($d = 200$ μm, $v = 1.0$ m/s), and (d) dimensionless surface temperature vs. Fourier number ($d = 200$ μm, $v = 1.0$ m/s).

Table 3
Equations of scaling laws for step heat flux input ($d = 200$ μm, $v = 1$ m/s)

Process variable	Scaling law
$\tau_i \times 10^6$	$3.315 - 7.826\theta_i + 3.354\theta_i^2$
$\tau_{vi} \times 10^6$	$6.350 - 10.884\theta_i + 4.152\theta_i^2$
$\tau_{max} \times 10^5$	$11.882 + 2.182\theta_i + 2.176\theta_i^2$
$\tau_{tot} \times 10^5$	$17.422 + 9.021\theta_i + 38.577\theta_i^2$
$\zeta_{max} \times 10^3$	$9.44 + 4.91\theta_i + 2.71\theta_i^2$
$\zeta_{v,max} \times 10^3$	$4.31 + 1.60\theta_i - 0.066\theta_i^2$

dimensionless substrate temperatures. A subsequent paper will treat the case of time-dependent heat flux input.

Table 4
Summary table for step heat flux input

Process variable	Dominant control parameter
τ_i	q''
τ_{vi}	Q_s
τ_{max}	τ
τ_{tot}	Q_s (without vaporization)
	$x_{vf,max}$ (with vaporization)
ζ_{max}	Q_s
$\zeta_{v,max}$	Q_s

Acknowledgement

This work was supported by National Science Foundation Grant DMI 0115205.

References

[1] S. Ahn, J. Murphy, J. Ramos, J.J. Beaman, Physical modeling for dynamic control of melting process in direct-SLS, in: H.L. Marcus, J.J. Beaman, J.W. Barlow, D.L. Bourell, R.H. Crawford (Eds.), Solid Freeform Fabrication Symposium Proceedings, The University of Texas at Austin, 2001.

[2] V. Alexiades, A.D. Solomon, Mathematical Modeling of Melting and Freezing Processes, Hemisphere Publishing Corporation, 1993.

[3] M. Bertolotti, C. Sibilia, Depth and velocity of the laser-melted front from an analytical solution of the heat conduction equation, IEEE J. Quantum Electron. QE-17 (10) (1981) 1980–1988.

[4] M. Bhattacharya, T. Basak, K.G. Ayappa, A fixed-grid finite element based enthalpy formulation for generalized phase change problems: role of superficial mushy region, Int. J. Heat Mass Transfer 45 (2002) 4881–4898.

[5] E.M. Breinan, B.H. Kear, Rapid solidification laser processing at high power density, in: M. Bass (Ed.), Laser Materials Processing, North-Holland Publishing Company, 1983, pp. 235–295.

[6] Y. Cao, A. Faghri, A numerical analysis of phase-change problems including natural convection, J. Heat Transfer 112 (1990) 812–816.

[7] C.K. Chun, S.O. Park, A fixed-grid finite-difference method for phase-change problems, Numer. Heat Transfer, Part B 38 (2000) 59–73.

[8] H. Chung, S. Das, Scaling laws for melting and resolidification in direct selective laser sintering of metals, in: H.L. Marcus, J.J. Beaman, J.W. Barlow, D.L. Bourell, R.H. Crawford (Eds.), Solid Freeform Fabrication Symposium Proceedings, The University of Texas at Austin, 2001.

[9] H.E. Cline, T.R. Anthony, Heat treating and melting material with a scanning laser or electron beam, J. Appl. Phys. 48 (9) (1977) 3895–3900.

[10] M.I. Cohen, Melting of a half-space subjected to a constant heat input, J. Franklin Inst. 283 (4) (1967) 271–285.

[11] S. Das, Direct selective laser sintering of high performance metals-machine design, Process Development and Process Control, Ph.D. thesis, University of Texas, Austin, TX, 1998.

[12] S. Das, H. Chung, A model of laser-powder interaction in direct selective laser sintering of metals, in: H.L. Marcus, J.J. Beaman, J.W. Barlow, D.L. Bourell, R.H. Crawford (Eds.), Solid Freeform Fabrication Symposium Proceedings, The University of Texas at Austin, 2001.

[13] C.R. Deckard, Selective laser sintering, Ph.D. thesis, University of Texas, Austin, TX, 1988.

[14] M.K. El-Adawi, E.F. Elshehawey, Heating a slab induced by a time-dependent laser irradiance-An exact solution, J. Appl. Phys. 60 (7) (1986) 2250–2255.

[15] J.R. Ho, C.P. Grigoropoulos, Computational study of heat transfer and gas dynamics in the pulsed laser evaporation of metals, J. Appl. Phys. 78 (7) (1995) 4696–4709.

[16] L.J. Huang, P.S. Ayyaswamy, I.M. Cohen, Melting and solidification of thin wires: a class of phase-change problems with a mobile interface—l. Analysis, Int. J. Heat Mass Transfer 38 (9) (1995) 1637–1645.

[17] D. Juric, G. Tryggvason, A front-tracking method for dendritic solidification, J. Comput. Phys. 123 (1996) 127–148.

[18] M.K. Moallemi, R. Viskanta, Analysis of melting around a moving heat source, Int. J. Heat Mass Transfer 29 (8) (1986) 1271–1282.

[19] H.G. Landau, Heat conduction in a melting solid, Quart. Appl. Math. 8 (1950) 80–94.

[20] J. Pak, O.A. Plumb, Melting in a two-component packed bed, J. Heat Transfer 119 (1997) 553–559.

[21] S.V. Patankar, Numerical Heat Transfer and Fluid Flow, Taylor and Francis, 1980.

[22] B. Podolsky, A problem in heat conduction, J. Appl. Phys. 22 (5) (1951) 581–585.

[23] A.M. Prokhorov, V.I. Konov, I. Ursu, I.N. Mihailescu, Laser Heating of Metals, Adam Hilger, 1990.

[24] D. Rosenthal, The theory of moving sources of heat and its application to metal treatments, Trans. ASME (1946) 849–866.

[25] N. Shamsundar, E.M. Sparrow, Analysis of multidimensional conduction phase change via the enthalpy model, J. Heat Transfer (1975) 333–340.

[26] O.P. Sharma, M. Rotenberg, S.S. Penner, Phase-change problems with variable surface temperature, AIAA J. 5 (4) (1967) 677–682.

[27] M. Shiomi, A. Yoshidome, F. Abe, K. Osakada, Finite element analysis of melting and solidifying processes in laser rapid prototyping of metallic powders, Int. J. Mach. Tools Manufacture 39 (1999) 237–252.

[28] B.D. Vujanovic, S.E. Jones, Approximate solutions of canonical heat conduction equations, J. Heat Transfer 112 (1990) 836–842.

[29] G.X. Wang, E.F. Matthys, Numerical modelling of phase change and heat transfer during rapid solidification processes: use of control volume integrals with element subdivision, Int. J. Heat Mass Transfer 35 (1) (1992) 141–153.

[30] G.X. Wang, V. Prasad, E.F. Matthys, An interface-tracking numerical method for rapid planar solidification of binary alloys with application to microsegregation, Mater. Sci. Eng. A 225 (1997) 47–58.

[31] S.P. Wang, G.X. Wang, E.F. Matthys, Melting and resolidification of a substrate in contact with a molten metal: operational maps, Int. J. Heat Mass Transfer 41 (10) (1998) 1177–1188.

[32] R.F. Wood, G.A. Geist, Modeling of nonequilibrium melting and solidification in laser-irradiated materials, Phys. Rev. B 34 (4) (1986) 2606–2620.

[33] J. Xie, A. Kar, Mathematical modeling of melting during laser materials processing, J. Appl. Phys. 81 (7) (1997) 3015–3022.

[34] X. Xu, C.P. Grigoropoulos, R.E. Russo, Heat transfer in excimer laser melting of thin polysilicon layers, J. Heat Transfer 117 (1995) 708–715.

[35] B.S. Yilbas, M. Sami, H.I. AbuAlHamayel, 3-dimensional modeling of laser repetitive pulse heating: a phase change and a moving heat source considerations, Appl. Surf. Sci. 134 (1998) 159–178.

[36] Y. Zhang, A. Faghri, Melting and resolidification of a subcooled mixed powder bed with moving gaussian heat source, J. Heat Transfer 120 (1998) 391–883.
[37] Y. Zhang, A. Faghri, Melting of a subcooled mixed powder bed with constant heat flux heating, Int. J. Heat Mass Transfer 42 (1999) 775–788.
[38] Y. Zhang, A. Faghri, Vaporization, melting and heat conduction in the laser drilling process, Int. J. Heat Mass Transfer 42 (1999) 1775–1790.
[39] T.F. Zien, Approximate calculation of transient heat conduction, AIAA J. 14 (3) (1976) 404–406.
[40] T.F. Zien, Integral solutions of ablation problems with time-dependent heat flux, AIAA J. 16 (12) (1978) 1287–1295.